

Endothermic Charge Separation Occurs Spontaneously in Non-Fullerene Acceptor/Polymer Bulk Heterojunction

Kushal Rijal,^{1,*} Neno Fuller,¹ Fatimah Rudayni,^{1,2} Nan Zhang,³ Xiaobing Zuo,⁴ Cindy L. Berrie,⁵ Hin-Lap Yip,^{3,6,7} Wai-Lun Chan^{1,*}

1. Department of Physics and Astronomy, University of Kansas, Lawrence, Kansas 66045, USA
2. Department of Physics, Jazan University, Jazan 45142, Saudi Arabia
3. Department of Materials Science and Engineering, City University of Hong Kong, Tat Chee Avenue, Kowloon, Hong Kong
4. X-ray Science Division, Argonne National Laboratory, Lemont, Illinois 60439, USA
5. Department of Chemistry, University of Kansas, Lawrence, Kansas 66045, USA
6. School of Energy and Environment, City University of Hong Kong, Tat Chee Avenue, Kowloon, Hong Kong
7. Hong Kong Institute for Clean Energy, City University of Hong Kong, Tat Chee Avenue, Kowloon, Hong Kong

Abstract:

Organic photovoltaics (OPVs) based on non-fullerene acceptors (NFAs) have achieved a power conversion efficiency close to 20%. These NFA OPVs can generate free carriers efficiently despite a very small energy level offset at the donor/acceptor (D/A) interface. Why these NFAs can enable efficient charge separation (CS) with low energy losses remains an open question. Here, the CS process in the PM6:Y6 bulk heterojunction (BHJ) is probed by time-resolved two-photon photoemission (TR-TPPE) spectroscopy. We found that the CS, the conversion from bound charge transfer (CT) excitons to free carriers, is an endothermic process with an enthalpy barrier of 0.15 eV. Interestingly, the CS can occur spontaneously despite being an endothermic process, which implies that it is driven by entropy. We further argue that the morphology of the PM6:Y6 film and the anisotropic electron delocalization restrict the electron and hole wavefunctions within the CT exciton such that they can only contact each other through point-like junctions. This configuration can maximize the entropic driving force.

* Email: kushalko85@ku.edu, wlchan@ku.edu

1. Introduction

Fullerene and its derivatives have long been used as the electron acceptor in organic photovoltaics (OPVs). However, despite decades of research and optimization, the efficiency of fullerene based OPVs plateaued at $\sim 12\%$ in the early 2010s,¹ which was significantly lower than the efficiency of photovoltaics made with other materials such as silicon and halide perovskites. This paradigm is shifted by the recent introduction of the Y-series non-fullerene acceptors (NFA), which results in a rapid increase in the OPVs efficiency towards $\sim 20\%$ in just a few years.²⁻¹¹ In high performing NFA/polymer bulk heterojunctions (BHJs), free carriers can be generated efficiently even when the energy offset between the singlet (S_1) exciton in the NFA and the charge transfer (CT) exciton is as small as ~ 0.1 eV,¹²⁻¹⁵ which significantly reduces the energy loss from the initial CT process at the donor/acceptor (D/A) interface. By contrast, for fullerene/polymer BHJs, a much larger energy offset (> 0.3 eV)^{1, 16} is often required to produce a high charge separation (CS) yield. Moreover, NFA based OPVs generally have a lower non-radiative recombination loss compared to fullerene based OPVs,^{14, 17, 18} which can be attributed to the long carrier lifetime found in NFA/polymer BHJs.^{9, 19} The low energy losses in both initial CT and charge extraction processes lead to a high open circuit voltage and the record-breaking power conversion efficiency.

While various mechanisms, such as the inhibition of triplet formation,^{9, 20} have been proposed to explain the long carrier lifetime in NFA OPVs, it is less clear why free carriers can be generated efficiently in the first-place despite the very small S_1 -CT energy offset. It is known that an electron-hole pair at the D/A interface is bound together to form a CT exciton, which can have a binding energy as large as ~ 0.5 eV.²¹⁻²³ Electron/hole delocalization would reduce this binding energy by forming the so-called hot CT excitons.²⁴⁻²⁷ However, when the energy offset at the D/A

interface is small, the initial CT transfer process cannot provide enough excess energy to populate such hot CT excitons, and CS needs to proceed *via* more localized and bound cold CT excitons. Mechanisms that allow the dissociation of cold CT excitons often rely on the extraction of electrons/holes by some lower energy sites originated from interfacial molecular mixing,²⁸⁻³² energetic disorders,^{33,34} or polaron formation.³⁵ These lower energy sites provide a gradient in the potential energy counteracting the CT exciton binding energy, but they unavoidably lead to a decrease in the potential energy of the separated carrier. Hence, these mechanisms intrinsically lead to energy losses. While details for each of these mechanisms can be very different, a simplistic view is that if a CT exciton is bound, one must pay the energy price to separate it into free carriers. Hence, it is counterintuitive that OPVs consisting of NFAs seemingly defy this basic rule and produce free carriers at a much lower energy loss.

In this work, we investigate the CS process in a representative NFA/polymer blend that is known as the Y6/PM6, which was responsible for the breakthrough in the OPV efficiency from ~12% to ~16%. We note that this NFA/polymer blend has been investigated previously by time-resolved optical pump-probe spectroscopy.^{19, 36-39} Here, time-resolved two photon photoemission spectroscopy (TR-TPPE) is employed, which allows us to measure the energy of the excited electron directly. By using this technique, we can trace the energy of the excited electron as a function of time during the CS process, which has not been captured by previous spectroscopy works. We found that CT excitons are generated within the first few picoseconds after the initial photoexcitation. Then, we observe a bifurcation of the CT exciton population into a higher energy charge separated state, and a lower energy trapped state. The CS process results in an enthalpy increase of ~ 150 meV. This observation is rather uncommon because excited electrons typically

lose energy to the environment instead of gaining energy from it. The observed enthalpy-uphill CS is also opposite to the typical hot exciton cooling observed in fullerene D/A interfaces.^{24-26, 40}

Our samples do not have any electrode for carrier extraction. Under this condition, excited electrons typically relax from higher energy states to lower energy ones as they equilibrate with the environment. Hence, the transfer of electrons from a lower to a higher energy state is counterintuitive. Indeed, by the principle of detailed balance, the steady-state population of the higher energy CS state should be orders of magnitude lower than that of the lower energy CT exciton state if we assume an energy difference of 0.15 eV. We propose that the endothermic CS process is driven by entropy. When the entropic driving force can compensate for the enthalpy increase, an endothermic process can proceed as if it is an energy downhill process. An entropy-driven CS process is also consistent with the athermal charge generation observed in NFA OPVs.⁴¹ The entropy-driven CS allows excitons to gain energy from the environment, which can intrinsically reduce energy loss compared to other CS mechanisms. We note that entropy-driven CS has been discussed in previous works,^{22, 42-44} but it remains unclear on what conditions the entropy mechanism can become dominant. Based on our recent works on model D/A interfaces,^{45, 46} and structural characterizations on PM6:Y6 BHJs, we will argue that the entropy driving force can be maximized in PM6:Y6 BHJs.

2. Results and Discussion

Before discussing our TR-TPPE results, we first establish the band alignment at the PM6:Y6 interface. Neat PM6 and Y6 films, and PM6:Y6 blends were spin-coated onto PEDOT:PSS/ITO substrates. The highest occupied molecular orbital (HOMO) of these samples is determined by ultraviolet photoemission spectroscopy (UPS). The UPS spectra for the three samples are shown in Fig. 1a. The energy in all the spectra is referenced with respect to the vacuum

level (E_v), in which the work function for each sample is determined from the secondary electron cutoff (SECO) of the spectrum (Fig. S1 in the supporting information). The HOMO peak is labelled in Fig. 1a. To determine the position of the HOMO peak more precisely, we subtract the inelastic photoelectron background from the spectrum (the subtracted spectra are provided in Fig. S2 in the supporting information). For neat PM6 and Y6 films, when HOMO levels of the two materials are aligned at the E_v , the PM6's and Y6's HOMOs almost have the same energy, with the Y6's HOMO lower than the PM6's HOMO by 0.12 eV. This offset is in very good agreement with reported HOMO offsets measured using cyclic voltammetry^{2, 47} and UPS spectroscopy.¹⁵ Because the HOMO offset is too small, we are not able to resolve the two different HOMO peaks in the BHJ film (the black curve in Fig. 1a). For the BHJ film, the measured HOMO will be treated as the average energy of the two HOMOs.

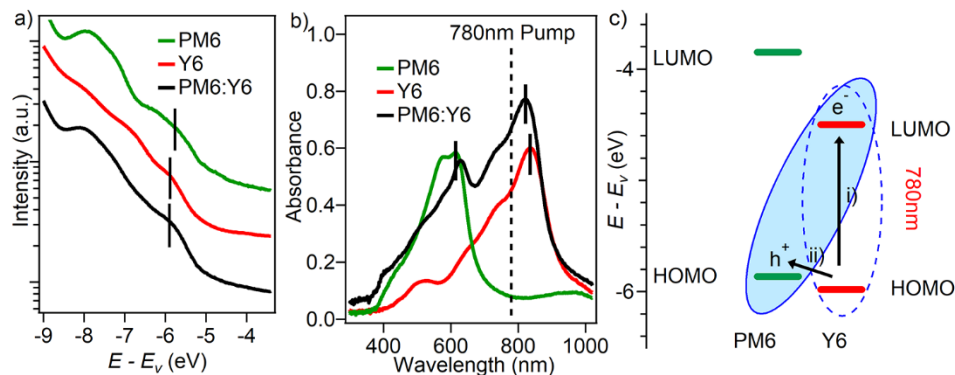


Figure 1: (a) UPS spectra of PM6, Y6, and PM6:Y6 films showing their HOMO peaks. (b) UV-vis absorption spectra of PM6, Y6, and PM6:Y6 films. (c) Schematic diagram showing type-II band alignment in the PM6:Y6 BHJ. In our TR-TPPE experiment, electrons in Y6's HOMO are excited to form S_1 excitons by the pump laser pulse (arrow i). Then, holes in Y6 can transfer to PM6 creating CT excitons (arrow ii).

The optical absorption spectra for the three samples are shown in Fig. 1b. The Y6 film has an absorption band in the 600 – 900 nm region with the lowest energy peak at ~ 836 nm (1.48 eV), while the PM6 film has an absorption band in the 500 – 700 nm region with the lowest energy peak at ~ 615 nm (2.02 eV). The absorption spectrum of the BHJ film consists of two absorption

bands originated from PM6 and Y6. We use the lowest energy peak as the optical band gap for the two materials. These band gaps, together with the HOMO offset measured by UPS, are used to draw the energy level diagram as shown in Fig. 1c. The PM6/Y6 interface has a type II band alignment as expected.

In our TR-TPPE experiment on the PM6:Y6 blend, singlet (S_1) excitons in Y6 are selectively excited by a pump pulse with a photon energy of 1.59 eV (arrow 'i' in Fig. 1c). This photon energy is much smaller than the PM6's band gap. Hence, the pump pulse cannot excite the S_1 exciton in PM6. Indeed, the control experiment done on the neat PM6 film does not show any pump-induced signal (Fig. S3 in the supporting information). Moreover, because of the type II band alignment, only holes in Y6 can be transferred to the PM6 (arrow 'ii' in Fig. 1c). This experimental design ensures that excited electrons always remain in Y6 domains. Excited electrons in Y6 are photoionized by a time-delayed UV probe pulse with a photon energy of 4.64 eV. The kinetic energy of the ionized electron is measured by the photoelectron spectrometer to obtain the TPPE spectrum. Although ionized electrons always originate from the lowest unoccupied molecular orbital (LUMO) of Y6, the kinetic energy of ionized electrons can be reduced by an amount equal to the exciton binding energy if the electron is bound by a hole. Hence, the TR-TPPE method allows us to resolve the energy difference between CT and CS states.^{40, 46, 48} Note that our experiment excites/detects the Y6 domain. To increase the photoemission signal, we used a PM6:Y6 blend with a weight ratio of 1:3 instead of the typical ratio of 1:1.2. Previous works have shown that changing the ratio to 1:3 only slightly lowers the power conversion efficiency.^{49, 50}

Figure 2a shows the TR-TPPE spectrum of the PM6:Y6 blend. The background photoemission signal from the negative delay-time is subtracted from the spectrum at each delay time to obtain the pump-induced two photon signal. This pump-induced signal corresponds to

photoelectrons originated from excited states. In the TPPE spectrum, the energy of the excited state (the intermediate state energy) is referenced with respect to the HOMO peak position obtained from the same sample, i.e. the $E - E_{HOMO}$ energy scale used in Fig. 2a. Because excited electrons reside in Y6 domains, the energy scale, $E - E_{HOMO}$, can also be written as:

$$E - E_{HOMO} = E_{LUMO}^{Y6} - E_{HOMO} - Ex_b, \quad (1)$$

where E_{LUMO}^{Y6} , E_{HOMO} , Ex_b are the Y6's LUMO energy, the average HOMO energy obtained from the UPS spectrum, and the exciton binding energy, respectively.

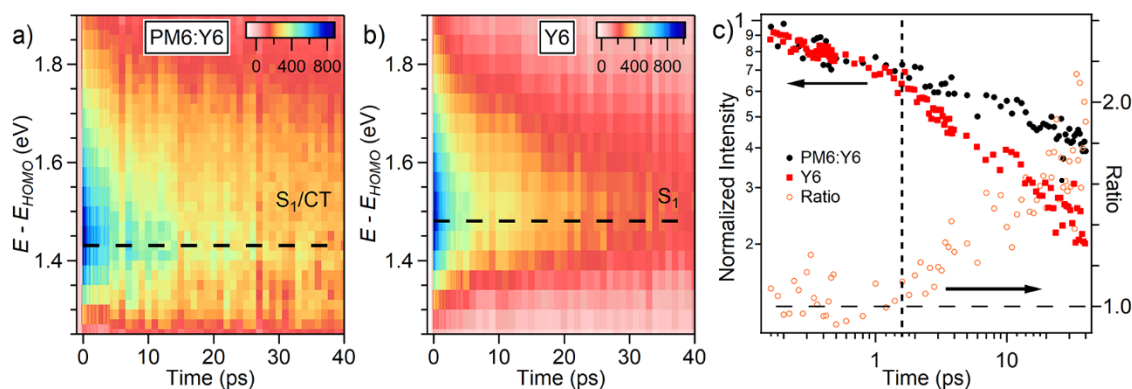


Figure 2: TR-TPPE spectra of (a) the PM6:Y6 blend, and (b) the neat-Y6 film for t up to 40 ps. (c) The integrated intensity of the two spectra as a function of time (solid symbols). The two samples have similar decay dynamics in the first 2 ps. However, the two curves diverge for $t > 2$ ps and the PM6:Y6 blend shows a slower decay rate. We attribute the slower intensity decay to the formation of CT excitons in the PM6:Y6 blend. The ratio of the two curves is also plotted (open symbol). This ratio starts to deviate from unity at $t \sim 2$ ps.

Near $t = 0$, a peak located at ~ 1.43 eV is observed (the dashed line in Fig. 2a). Because S_1 excitons in Y6 are populated directly by the pump pulse, the position of this peak should be roughly equal to the S_1 energy of Y6. Indeed, this energy is in good agreement with the lowest energy optical absorption peak of the PM6:Y6 blend (~ 1.51 eV in Fig. 1b). For comparison, the TR-TPPE spectrum of the neat Y6 film is shown in Fig. 2b. A peak at a similar position (~ 1.48 eV) is observed. This energy is slightly larger than that of the PM6:Y6 blend. For the PM6:Y6 blend, the HOMO peak obtained from the UPS spectrum is a convolution of the Y6's and PM6's HOMO

peak. Because the PM6's HOMO is at a slightly higher energy than the Y6's HOMO, E_{HOMO} used in Eq. (1) to calculate the exciton energy is higher than the actual Y6's HOMO. This explains why the S_1 energy appears to be lower in the PM6:Y6 spectrum.

Even though the same S_1 peak is observed in the neat Y6 films and the PM6:Y6 blend near $t = 0$, the signal decays differently for the two samples. Figure 2c shows the integrated intensity of the photoemission peak as a function of time. To compare the two curves, the intensity at $t = 0$ is normalized to one. The two decay curves show very similar dynamics up to $t \sim 2$ ps at which they begin to diverge. For $t > 2$ ps, the signal for the PM6:Y6 blend clearly shows a longer lifetime. We attribute this longer lifetime to the formation of CT excitons in the PM6:Y6 blend, which are expected to have a longer lifetime than Y6's S_1 excitons. The time at which the two curves diverge (~ 2 ps) should correspond to the average hole transfer time from Y6 to PM6. This hole transfer time agrees well with previous ultrafast measurements,^{36, 38, 51} which report a hole transfer time in the range of $\sim 0.2 - 10$ ps in PM6:Y6 BHJs. The transition can be visualized more clearly by taking the ratio of the two decay curves, which is shown as the open circles in Fig. 2c. The ratio begins to deviate from unity at $t \sim 2$ ps.

Note that in our TPPE spectrum (Fig. 2a), we do not notice significant shift in the peak position at $t \sim 2$ ps, which suggests that S_1 and CT excitons have a very similar exciton binding energy. This is because the measured energy (E in Eq. (1)) is equal to $E_{LUMO}^{Y6} - Ex_b$. Indeed, the difference between exciton binding energies of S_1 and CT excitons ($\Delta Ex_b^{S_1-CT}$) can be expressed as (see Supporting information, Sec. III):

$$\Delta Ex_b^{S_1-CT} = (E_{HOMO}^{PM6} - E_{HOMO}^{Y6}) - (E_{S_1}^{Y6} - E_{CT}). \quad (2)$$

In this equation, the $E_{HOMO}^{PM6} - E_{HOMO}^{Y6}$ term represents the HOMO offset between PM6 and Y6. $E_{S_1}^{Y6}$ and E_{CT} represents the energy of the Y6 S_1 exciton and the CT exciton, respectively. All energies

on the right side of Eq. (2) have been widely reported in the literature. Typically, $E_{HOMO}^{PM6} - E_{LUMO}^{Y6} \sim 0.1$ eV, $E_{S_1}^{Y6} \sim 1.4$ eV, and $E_{CT} \sim 1.3$ eV.^{2, 14, 15, 47} The two brackets on the right side of Eq. (2) roughly cancels each other, which gives $\Delta E x_b^{S_1-CT} \sim 0$ eV. Hence, the S_1 and CT peaks should appear at a very similar energy in the TPPE spectrum and cannot be resolved by our setup.

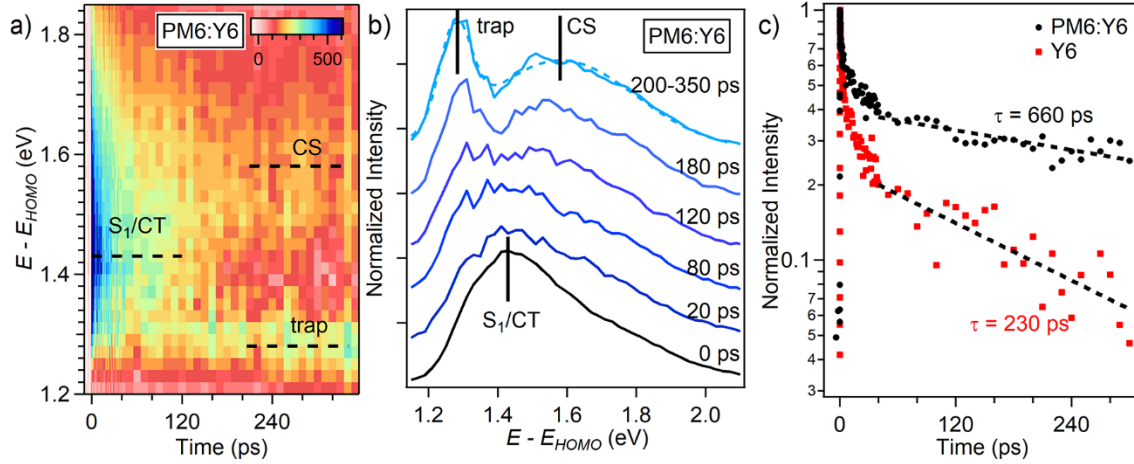


Fig. 3: (a) The TR-TPPE spectrum of the PM6:Y6 blend at longer delay times. The S_1/CT peak bifurcates into a higher energy CS state and a lower energy trap state. (b) The TPPE spectra at various delay times. To compare the spectral shape, we normalize each spectrum with its total area under the curve. The spectra are also offset vertically for clarity. (d) The normalized photoemission intensity as a function of time for the PM6:Y6 blend and the neat-Y6 film. The intensity decay for $t > 40$ ps is fitted with an exponential decay (dashed lines). The decay time constants (τ) are indicated on the figure.

Figure 3a shows the TR-TPPE spectrum for the PM6:Y6 blend at longer delay times. Interestingly, the S_1/CT peak bifurcates into two states at $t \sim 100$ ps. We attribute the higher and lower energy states to the CS state and a trap state, respectively. The trap state can be either trapped CT excitons or trapped Y6's S_1 excitons that cannot be converted into CT excitons in the first place. While it is typical that excitons funnel into lower energy sites at longer delay times, the conversion into a higher energy CS state is rather uncommon. Figure 3b shows a series of TPPE spectra at various delay times. All spectra are normalized by their respective total area, so that their spectral shape can be compared. The averaged spectrum from $t = 200 - 350$ ps (the topmost curve)

is fitted with two Gaussian functions (the fit is shown as the dashed line). Two peaks centered at ~ 1.58 eV (CS state) and ~ 1.28 eV (trap state) are found. The energy of the CS state is ~ 0.15 eV higher than the energy of the CT state. This energy difference can be attributed to the exciton binding energy of the CT exciton. We note that previous works have shown that the minimum separation between electron and hole in a localized CT exciton is ~ 22 Å.²⁷ By using a generic dielectric constant of ~ 4 , we can obtain a Coulomb potential energy of 0.16 eV, which agrees reasonably well with the observed CT exciton binding energy. Hence, our data suggests that the localized CT state, which is generated initially at the interface, dissociates into a free electron-hole pair spontaneously within ~ 100 ps (probably *via* some delocalized CT states). Although similar CS times (10 – 100 ps) have been reported in previous works,^{19, 38, 39} our measurement provides direct evidence that the CS process is an enthalpy uphill process.

The observation of an enthalpy uphill process is notable because our samples are not attached to any external electrodes for charge extraction. On the 1 – 100 ps timescale, excited electrons typically equilibrate with the environment by relaxing into lower energy states. By the principle of detailed balance, if the enthalpy change (ΔE) is the only contribution to the free energy change (ΔF), the ratio of the concentration of the higher enthalpy CS state to that of the lower enthalpy localized CT state should be given by $\exp(-\Delta E/k_B T)$, in which k_B and T are the Boltzmann constant and the temperature, respectively. In our case, $\Delta E \sim 0.15$ eV, which results in a ratio of $\sim 2.5 \times 10^{-3}$, i.e., the equilibrium concentration of the CS state should be ~ 3 orders of magnitude smaller than the localized CT state. This low concentration should make the higher energy CS state unobservable in our spectrum. Instead, our spectrum shows a spectral shift towards higher energies at longer delay times. Hence, terms other than ΔE must contribute significantly to ΔF . Because our film is not subjected to any external field that would have lowered the free energy of the CS

state, we conclude that the entropic driving force ($-T\Delta S$) should have a significant contribution to the free energy change ($\Delta F = \Delta E - T\Delta S$) in the CS process. If the $-T\Delta S$ can compensate ΔE , the CS process is essentially barrierless (in terms of free energy). This is consistent with a previous experimental observation that the energy barrier for charge generation appears to be zero near room temperature, but the barrier increases at lower temperatures.^{39,41} The barrier increase at lower temperatures can be explained by the diminishing of the entropy driving force ($T\Delta S$). Indeed, our measurement conducted at the low temperature (~ 170 K) does not show the enthalpy uphill CS process (Fig. S4, supporting information).

The same experiment was also performed on the neat Y6 film, and we do not observe any spectral shift other than a monotonic decay of the exciton population (see supporting information, Fig. S5). We note that some recent works have proposed that free carriers can be generated spontaneously in neat Y6 films.^{37, 52} However, our result does not show enthalpy-uphill CS occurring in neat Y6 films. Therefore, we believe that CS in PM6:Y6 blends mainly occurs at the D/A interface. Finally, we compare the signal decay dynamics between neat Y6 and PM6:Y6 films. For this purpose, the photoemission intensity is integrated across the whole spectral range to include all states with different energies. Figure 3c shows the temporal evolution of this integrated intensity, with the intensity at $t = 0$ normalized to one. In both samples, the population decays exponentially at $t > 40$ ps. The observed decay time constants for PM6:Y6 and neat-Y6 films are 660 ps, and 230 ps respectively. The longer lifetime observed in PM6:Y6 is consistent with the generation of free carriers in the PM6:Y6 film.

After showing that the enthalpy-uphill CS, likely to be driven by entropy, can occur in the PM6:Y6 blend, we proceed to another important question on what kind of morphology would enhance the entropic driving force. To this end, we have done structural characterizations on our

PM6:Y6 blend. Figure 4a shows the grazing incidence wide angle X-ray scattering (GIWAXS) pattern of the PM6:Y6 blend. GIWAXS patterns for other controlled samples, such as neat Y6, neat PM6 and PEDOT:PSS films, are provided in the supporting information (Fig. S6). The GIWAXS pattern shows a broad, isotropic diffraction ring at a wavevector (q) $\sim 1.56 \text{ \AA}^{-1}$, which can be observed when either the PM6 polymer or the PEDOT:PSS layer is present (Fig. S6). We assign this diffraction ring to the π - π stacking peak of the polymer film. The scattering intensity along the out-of-plane (vertical) and in-plane (horizontal) directions of the GIWAXS pattern of the PM6:Y6 blend are shown in Fig. 4b. In addition to the peak related to the diffraction ring (green line), another peak at $q \sim 1.78 \text{ \AA}^{-1}$ (3.53 \AA) can be observed in the out-of-plane direction (red line). This peak is observed only when Y6 is present. Hence, we assign this peak to the π - π stacking peak of Y6. This assignment is consistent with previous works.^{2, 27} The 1.78 \AA^{-1} peak only appears in the out-of-plane direction, which implies that Y6 molecules have a face-on orientation.

To measure the periodicity at smaller q (longer length scales), we employed the grazing incidence small angle X-ray scattering (GISAXS). The GISAXS pattern for the PM6:Y6 blend is shown in Fig. 4c, and GISAXS patterns for other controlled samples can be found in Fig. S7 in the supporting information. In the GISAXS pattern, an intense stripe can be found along the out-of-plane direction, which can be originated from the surface roughness. We will focus on the intensity cut along the in-plane direction, which shows clearer diffraction peaks. In the line cut along the in-plane direction (Fig. 4d), a peak at $\sim 0.29 \text{ \AA}^{-1}$ (d -spacing of 21.7 \AA) and a shoulder at $\sim 0.40 \text{ \AA}^{-1}$ (d -spacing of 15.7 \AA) can be found for the PM6:Y6 blend. The peak at $\sim 0.29 \text{ \AA}^{-1}$ can be contributed from both PM6 and Y6 because it can be found in both PM6 and Y6 neat films. However, the shoulder at $\sim 0.4 \text{ \AA}^{-1}$ is unique to Y6. Previous work has assigned this peak to the lamellar diffraction peak of Y6 which corresponds to the distance of the end group between two neighboring

Y6 stacks.²⁷ The appearance of the lamellar peak in the in-plane direction further confirms that Y6 molecules have a face-on orientation. We also plot the scattering intensity in the in-plane direction for very small q (Fig. 4e). On top of the monotonically decaying background, intensity bumps at different locations for different samples can be found (labelled by arrows). These linecuts can be fitted to obtain the PM6 and/or Y6 domain sizes (see supporting information, Fig. S8). The domain sizes obtained from the fit for the PM6:Y6, neat-PM6, and neat-Y6 films are 52 nm, 19 nm, and 113 nm, respectively. As we will show, very similar domain sizes can also be found from atomic force microscopy (AFM) images.

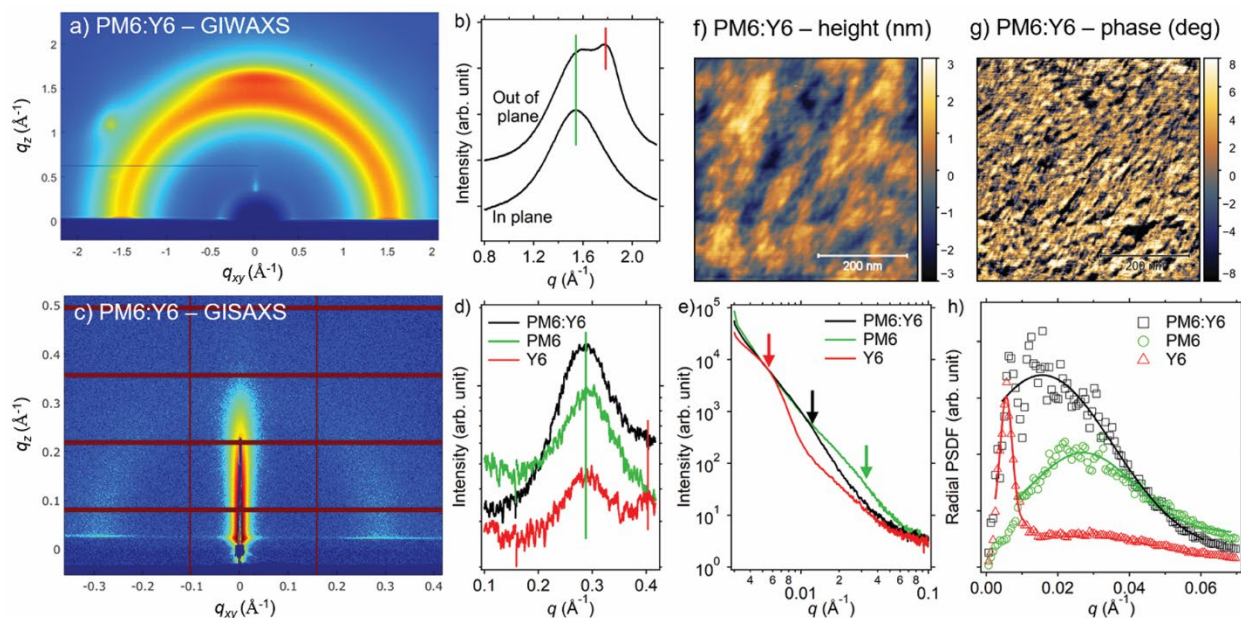


Figure 4: (a) The GIWAXS pattern for the PM6:Y6 blend. (b) The intensity cut for the pattern shown in (a) along the out-of-plane and in-plane directions. (c) The GISAXS pattern of the PM6:Y6 blend. (d, e) The intensity cut along the in-plane direction of GISAXS patterns of PM6:Y6, neat-PM6, and neat-Y6 films. (f) The AFM topology, and (g) phase images of the PM6:Y6 film. (h) Radial PSD functions calculated from phases images of PM6:Y6, neat-PM6, and neat-Y6 films.

Figure 4f and g show the topology and phase images of the PM6:Y6 blend measured by AFM. While the topology image provides information such as the surface roughness, the phase image can reveal features like grain and domain boundaries. In the phase image shown in Fig. 4g,

some fine, elongated features are observed which can be attributed to the nano-fibrous structure of the polymer network.^{5, 6, 10, 49} Intertwined fiber-like domains are even more clear in the phase image of the neat PM6 film (Fig. S9 in the supporting information). To determine the characteristic domain size of the structure, we calculate the radial power spectral density (r-PSD), i.e., the Fourier transform of the autocorrelation function, of the phase image. The r-PSD curves are shown in Fig. 4h. The peak positions of the r-PSD curves are found by fitting the peak with a Gaussian function. Domain sizes determined from the peak position are 40 nm (PM6:Y6), 23 nm (neat-PM6), and 112 nm (neat-Y6), which agrees well with those determined by GISAXS (52 nm for PM6:Y6, 19 nm for PM6, and 113 nm for Y6). The neat PM6 film shows a polymer network with the smallest periodicity of ~ 20 nm. For the PM6/Y6 blend, the contrast in the phase image is mainly contributed by the polymer network,^{5, 6, 10, 49} and the characteristic size is increased to $\sim 40 - 50$ nm. The polymer network appears to be enlarged as Y6 domains are incorporated into the polymer network. Finally, the phase image of the neat Y6 film does not show elongated fiber-like domains, and the ~ 100 nm length scale should correspond to the average grain size of the Y6 film.

The X-ray scattering and AFM images capture two important characteristics of the PM6:Y6 BHJ film. First, planar Y6 molecules stack in the direction perpendicular to the surface (captured by GIWAXS), and probably form some rod-like domains along the same direction due to the strong π - π coupling in this direction. Second, the PM6 forms nano-sizes bundles which intertwine with each other to form a mesh-like structure in which the polymer chain lays parallel to the substrate (captured by AFM) and the π - π stacking direction between polymer chains is either parallel or perpendicular to the surface (captured by GIWAXS). The two structural features are summarized schematically in Fig. 5a. In this figure, each domain consists of multiple stacks of Y6 molecules or multiple polymer chains. We note that the electron in the CT exciton primarily delocalizes along

the π -stacking direction in the Y6 stack and the hole primarily delocalizes along the PM6-polymer chain. To illustrate how the CT exciton would look like, in Fig. 5b, we only draw a stack of Y6 molecules and a PM6 polymer chain that touches each other. Because the polymer chain and the Y6-stack are oriented in different directions, the CT exciton can only be formed at the intersection point where the two domains met. As a result, the delocalized electron and hole in the CT excitons can only intersect with each other through a point-like junction (Fig. 5b), which has a minimal contact area. The contact area between electron and hole wavefunctions can further be reduced by bulky and irregular side-groups of the Y6 and PM6, which tends to isolate the core of the Y6 from that of the PM6.

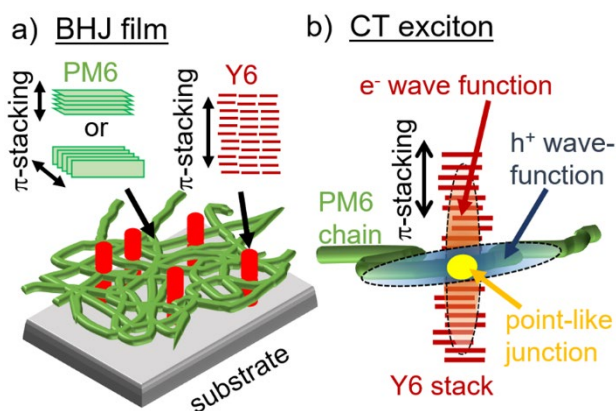


Figure 5: Schematic diagrams showing (a) the morphology of the PM6:Y6 film, and (b) the delocalized electron and hole wavefunctions within the CT exciton. In (a), each domain consists of multiple stacks of Y6 molecules or multiple polymer chains. The morphology of the PM6:Y6 allows the electron and hole wavefunctions within the CT exciton to form a point-like junction, which can maximize the entropic driving force.

Previously, we have investigated the CS dynamics in several model D/A interfaces with various molecular orientations, and with fullerene and non-fullerene-planar electron acceptors.^{40, 45, 46, 53, 54} We found that the enthalpy-uphill CS occurs only at interfaces where the delocalized electron and hole form point-like junctions.^{45, 46, 53} For other interfaces, the more conventional hot CT-exciton cooling is observed.^{26, 40, 45, 54} By using a tight-binding Hamiltonian, we previously

modeled the density of CT/CS states at different interfaces as a function of the energy.^{45, 46} We found that a point-like contact can suppress the density of localized CT states relative to the density of delocalized ones. Hence, the density of state for CT/CS states can increase more rapidly with the energy, which can increase the entropic driving force. Likewise, in the case of PM6:Y6, the combination of morphology and anisotropic electron delocalization restricts the delocalized electron and hole to contact *via* isolated point-like junctions. This structural feature can promote spontaneous enthalpy uphill CS because it enlarges the entropic driving force.

Finally, we note that while entropic driving force is often discussed in terms of its role in facilitating CS, it could reduce the recombination rate as well. This is because the entropic driving force, if it is large enough ($T\Delta S > \Delta E$), can become a barrier for the reverse of the CS process – the recombination of electron-hole pairs back to CT excitons. Because a CT exciton is a precursor for the electron-hole recombination, a large enough entropic driving force can suppress the bimolecular recombination rate and increase the carrier lifetime. This can explain the long carrier lifetime often observed in NFA BHJs.^{9, 19, 36} An increased carrier lifetime can in turn reduce the recombination loss in the open circuit voltage and improve the overall power conversion efficiency.

3. Conclusion

In conclusion, we have shown that the CS process in PM6:Y6 BHJs is an endothermic process with an enthalpy barrier of ~ 0.15 eV. The CS can occur spontaneously within 100 ps without any external field despite it is an enthalpy-uphill process. This observation is in contrast with many proposed CS mechanisms, which are based on arguments that either the enthalpy barrier is absent, or charges are extracted from CT excitons by sites with lower potential energies. Our result shows that an enthalpy barrier is indeed present, but it would be overcome spontaneously by

the entropy driving force. We further propose that the entropy driving force is enhanced in NFA/polymer BHJs because its morphology and structural anisotropy prohibit delocalized electron and hole wavefunctions within the CT excitons to form an extensive spatial contact. The two electronic wavefunctions in the CT exciton can only be in contact with each other through some point-like junctions, which can significantly reduce the density of localized CT states relative to delocalized ones and enhance the entropic driving force. An entropy-driven CS is intrinsically an energy gain process as it allows a CT exciton to gain energy from the thermal bath. Therefore, it can uniquely account for the very low energy loss observed in recent NFA OPVs.

4. Experimental Section

Sample preparation – Reagents and chemicals were purchased directly from commercial vendors. PM6 and Y6 were obtained from Solarmer Energy, Inc. For optical absorption, AFM, UPS, and TR-TPPE measurements, the organic films were fabricated on PEDOT:PSS/ITO/glass. Initially, ITO/glass substrates were subjected to ultrasonic cleaning using detergent, DI water, acetone, and IPA for a duration of 15 minutes each. After the cleaning process, substrates were dried with N₂ gas. Then, they were placed in an oven at 80°C for 20 minutes for further drying. Finally, ITO/glass substrates were treated by O₂ plasma for 10 minutes, before transferring to a N₂-glove box for spin-coating. PEDOT:PSS (Sigma-Aldrich, conductive grade, 483095) was spin-coated onto the substrates at a speed of 4000 rpm for 1 minute. The coated substrates were then baked on a hot plate at 150°C for 20 minutes. The PM6:Y6 blend solution was prepared in chloroform with a mixing weight ratio of 1:3. The total concentration was kept at 16 mg/mL. Similarly, for neat-PM6 and neat-Y6 films, the solution was prepared in chloroform with a concentration of 8 mg/mL. Solutions were stirred at 40°C for 3 hours before being spin-coated

onto the PEDOT: PSS layer at a speed of 2500 rpm for 40 seconds. Finally, samples were annealed at 110°C for 10 minutes, completing the fabrication process.

UPS experiments – All photoemission spectroscopy experiments were done in an ultra-high vacuum (UHV) chamber with a base pressure of $\sim 1 \times 10^{-10}$ Torr. A standard UV lamp was used to generate UV light for the UPS measurement. The He-I emission line, which has a photon energy of 21.22 eV, was used in our experiment. The energy and emission angle of the photoelectrons were measured using a hemispherical analyzer equipped with an imaging detector (Phoibos 100, SPECS).

TR-TPPE experiment – The energy and population of the excited states were measured using a pump-probe approach. The pump beam had a photon energy of 1.59 eV, while the time-delayed probe beam had a photon energy of 4.64 eV. The pump and probe beams were generated from the outputs of two noncollinear optical parametric amplifiers (NOPAs), Light Conversion Orpheus-N-2H and Orpheus-N-3H, which were pumped by a Yb:KGW regenerative amplifier running at 125 kHz (Light Conversion, Pharos 10 W). The pump and probe pulses had pulse durations of 25 and 65 fs, respectively. The full width at half maximum (fwhm) of the Gaussian profile (pulse energy) of the pump and probe pulses at the sample were 1.0 mm (132 nJ) and 0.85 mm (2 nJ), respectively. At an incidence angle of 30°, the peak fluence at the center of the pump beam is 10.1 $\mu\text{J cm}^{-2}$. We estimate that an initial excitation density of $6.2 \times 10^{18} \text{ cm}^{-3}$ is produced by a pump pulse by using the optical constants reported in Ref. [55] (see supporting information, Sec. VI). The kinetic energy of the emitted photoelectrons was measured using a hemispherical electron analyzer equipped with an imaging detector (Phoibos 100, SPECS).

GIWAXS/GISAXS measurement – The grazing incidence small-angle and wide-angle x-ray scattering measurements were performed at Beamline 12-ID-B of the Advanced Photon Source

(APS) at Argonne National Laboratory (Lemont, IL). An Eiger2 9M detector (DECTRIS) was used for GISAXS measurements and the sample-to-detector distance was set 2.0 meters. The GIWAXS data were collected using a Perkin Elmer XRpad detector with the sample-to-detector distance of ca. 180 mm. The X-ray energy was 13.3 keV for both GISAXS and GIWAXS measurements. The linecuts were done using the beamline software. To avoid the diffraction peaks originated from the ITO substrate, the samples used for X-ray measurements were fabricated SiO₂ (300 nm)/Si wafer instead of ITO/glass using the same procedure outlined above.

AFM measurement and analysis – AFM measurements were obtained using a Digital Instruments Multimode Nanoscope IIIA instrument. Tapping mode images were collected using NSC35 probe tips (NanoAndMore) with a resonance frequency of ~150 kHz with a 1 Hz scan rate. Images were collected at 3-5 locations on each sample at multiple different scan sizes ranging from 500 nm to 5 μ m. The r-PSD functions are calculated by the open-source program Gwyddion (<http://gwyddion.net/>). The average of the r-PSD functions calculated from three 1 μ m \times 1 μ m images collected from different areas was used.

Acknowledgement:

This material is based upon work supported by the U.S. Department of Energy, Office of Science, Office of Basic Energy Sciences, Chemical Sciences, Geosciences, and Biosciences Division under Award Number DE-SC0024525. W. L. C. also acknowledges the support from the University of Kansas General Research Fund allocation #2151080. C. L. B. was supported by the National Science Foundation under award CHE-2108448 as well as the University of Kansas General Research Fund # 2112080. F.R. acknowledges the scholarship support from Jazan University. This research used the beamline 12-ID-B of the Advanced Photon Source, a U.S. Department of Energy (DOE) Office of Science user facility at Argonne National Laboratory and is based on research supported by the U.S. DOE Office of Science-Basic Energy Sciences, under Contract No. DE-AC02-06CH11357. H.-L. Y acknowledges the support from the University Grants Committee of Hong Kong (GRF 11307323).

References:

- (1) Scharber, M. C.; Sariciftci, N. S. Efficiency of bulk-heterojunction organic solar cells. *Prog. Polym. Sci.* **2013**, *38*, 1929-1940.
- (2) Yuan, J.; Zhang, Y. Q.; Zhou, L. Y.; Zhang, G. C.; Yip, H. L.; Lau, T. K.; Lu, X. H.; Zhu, C.; Peng, H. J.; Johnson, P. A.; Leclerc, M.; Cao, Y.; Ulanski, J.; Li, Y. F.; Zou, Y. P. Single-Junction Organic Solar Cell with over 15% Efficiency Using Fused-Ring Acceptor with Electron-Deficient Core. *Joule* **2019**, *3*, 1140-1151.
- (3) Lin, F.; Jiang, K.; Kaminsky, W.; Zhu, Z. L.; Jen, A. K. Y. A Non-fullerene Acceptor with Enhanced Intermolecular pi-Core Interaction for High-Performance Organic Solar Cells. *J. Am. Chem. Soc.* **2020**, *142*, 15246-15251.
- (4) Lin, Y. B.; Firdaus, Y.; Isikgor, F. H.; Nugraha, M. I.; Yengel, E.; Harrison, G. T.; Hallani, R.; El-Labban, A.; Faber, H.; Ma, C.; Zheng, X. P.; Subbiah, A.; Howells, C. T.; Bakr, O. M.; McCulloch, I.; De Wolf, S.; Tsetseris, L.; Anthopoulos, T. D. Self-Assembled Monolayer Enables Hole Transport Layer-Free Organic Solar Cells with 18% Efficiency and Improved Operational Stability. *ACS Energy Lett.* **2020**, *5*, 2935-2944.
- (5) Liu, Q. S.; Jiang, Y. F.; Jin, K.; Qin, J. Q.; Xu, J. G.; Li, W. T.; Xiong, J.; Liu, J. F.; Xiao, Z.; Sun, K.; Yang, S. F.; Zhang, X. T.; Ding, L. M. 18% Efficiency organic solar cells. *Sci. Bull.* **2020**, *65*, 272-275.
- (6) Cui, Y.; Yao, H.; Zhang, J.; Xian, K.; Zhang, T.; Hong, L.; Wang, Y.; Xu, Y.; Ma, K.; An, C.; He, C.; Wei, Z.; Gao, F.; Hou, J. Single-Junction Organic Photovoltaic Cells with Approaching 18% Efficiency. *Adv. Mater.* **2020**, *32*, 1908205.
- (7) Li, C.; Zhou, J. D.; Song, J. L.; Xu, J. Q.; Zhang, H. T.; Zhang, X. N.; Guo, J.; Zhu, L.; Wei, D. H.; Han, G. C.; Min, J.; Zhang, Y.; Xie, Z. Q.; Yi, Y. P.; Yan, H.; Gao, F.; Liu, F.; Sun, Y. M. Non-fullerene acceptors with branched side chains and improved molecular packing to exceed 18% efficiency in organic solar cells. *Nat. Energy* **2021**, *6*, 605-613.
- (8) Meng, H. F.; Liao, C. T.; Deng, M.; Xu, X. P.; Yu, L. Y.; Peng, Q. 18.77 % Efficiency Organic Solar Cells Promoted by Aqueous Solution Processed Cobalt(II) Acetate Hole Transporting Layer. *Angew Chem. Int. Ed.* **2021**, *60*, 22554-22561.
- (9) Jiang, K.; Zhang, J.; Zhong, C.; Lin, F. R.; Qi, F.; Li, Q.; Peng, Z. X.; Kaminsky, W.; Jang, S. H.; Yu, J. W.; Deng, X.; Hu, H. W.; Shen, D.; Gao, F.; Ade, H.; Xiao, M.; Zhang, C. F.; Jen, A. K. Y. Suppressed recombination loss in organic photovoltaics adopting a planar-mixed heterojunction architecture. *Nat. Energy* **2022**, *7*, 1076-1086.
- (10) Zhu, L.; Zhang, M.; Xu, J. Q.; Li, C.; Yan, J.; Zhou, G. Q.; Zhong, W. K.; Hao, T. Y.; Song, J. L.; Xue, X. N.; Zhou, Z. C.; Zeng, R.; Zhu, H. M.; Chen, C. C.; MacKenzie, R. C. I.; Zou, Y. C.; Nelson, J.; Zhang, Y. M.; Sun, Y. M.; Liu, F. Single-junction organic solar cells with over 19% efficiency enabled by a refined double-fibril network morphology. *Nat. Mater.* **2022**, *21*, 656-663.
- (11) Zhang, M.; Zhu, L.; Zhou, G. Q.; Hao, T. Y.; Qiu, C. Q.; Zhao, Z.; Hu, Q.; Larson, B. W.; Zhu, H. M.; Ma, Z. F.; Tang, Z.; Feng, W.; Zhang, Y. M.; Russell, T. P.; Liu, F. Single-layered organic photovoltaics with double cascading charge transport pathways: 18% efficiencies. *Nat. Commun.* **2021**, *12*, 309.
- (12) Qian, D. P.; Zheng, Z. L.; Yao, H. F.; Tress, W.; Hopper, T. R.; Chen, S. L.; Li, S. S.; Liu, J.; Chen, S. S.; Zhang, J. B.; Liu, X. K.; Gao, B. W.; Ouyang, L. Q.; Jin, Y. Z.; Pozina, G.; Buyanova, I. A.; Chen, W. M.; Ingnas, O.; Coropceanu, V.; Bredas, J. L.; Yan, H.; Hou, J. H.; Zhang, F. L.; Bakulin, A. A.; Gao, F. Design rules for minimizing voltage losses in high-efficiency organic solar cells. *Nat. Mater.* **2018**, *17*, 703-709.

- (13) Chen, S. S.; Wang, Y. M.; Zhang, L.; Zhao, J. B.; Chen, Y. Z.; Zhu, D. L.; Yao, H. T.; Zhang, G. Y.; Ma, W.; Friend, R. H.; Chow, P. C. Y.; Gao, F.; Yan, H. Efficient Nonfullerene Organic Solar Cells with Small Driving Forces for Both Hole and Electron Transfer. *Adv. Mater.* **2018**, *30*, 1804215.
- (14) Karki, A.; Vollbrecht, J.; Dixon, A. L.; Schopp, N.; Schrock, M.; Reddy, G. N. M.; Nguyen, T. Q. Understanding the High Performance of over 15% Efficiency in Single-Junction Bulk Heterojunction Organic Solar Cells. *Adv. Mater.* **2019**, *31*, 1903868.
- (15) Wan, P.; Chen, X. T.; Liu, Q.; Mahadevan, S.; Guo, M. X.; Qiu, J. J.; Sun, X. J.; Tsang, S. W.; Zhang, M. J.; Li, Y. F.; Chen, S. Direct Observation of the Charge Transfer States from a Non-Fullerene Organic Solar Cell with a Small Driving Force. *J. Phys. Chem. Lett.* **2021**, *12*, 10595-10602.
- (16) Coffey, D. C.; Larson, B. W.; Hains, A. W.; Whitaker, J. B.; Kopidakis, N.; Boltalina, O. V.; Strauss, S. H.; Rumbles, G. An Optimal Driving Force for Converting Excitons into Free Carriers in Excitonic Solar Cells. *J. Phys. Chem. C* **2012**, *116*, 8916-8923.
- (17) Liu, X.; Li, Y. X.; Ding, K.; Forrest, S. Energy Loss in Organic Photovoltaics: Nonfullerene Versus Fullerene Acceptors. *Phys. Rev. Appl.* **2019**, *11*, 024060.
- (18) Azzouzi, M.; Yan, J.; Kirchartz, T.; Liu, K. K.; Wang, J. L.; Wu, H. B.; Nelson, J. Nonradiative Energy Losses in Bulk-Heterojunction Organic Photovoltaics. *Phys. Rev. X* **2018**, *8*, 031055.
- (19) Hinrichsen, T. F.; Chan, C. C. S.; Ma, C.; Palecek, D.; Gillett, A.; Chen, S. S.; Zou, X. H.; Zhang, G. C.; Yip, H. L.; Wong, K. S.; Friend, R. H.; Yan, H.; Rao, A.; Chow, P. C. Y. Long-lived and disorder-free charge transfer states enable endothermic charge separation in efficient non-fullerene organic solar cells. *Nat. Commun.* **2020**, *11*, 5617.
- (20) Gillett, A. J.; Privitera, A.; Dilmurat, R.; Karki, A.; Qian, D. P.; Pershin, A.; Londi, G.; Myers, W. K.; Lee, J.; Yuan, J.; Ko, S. J.; Riede, M. K.; Gao, F.; Bazan, G. C.; Rao, A.; Nguyen, T. Q.; Beljonne, D.; Friend, R. H. The role of charge recombination to triplet excitons in organic solar cells. *Nature* **2021**, *597*, 666-671.
- (21) Bredas, J. L.; Norton, J. E.; Cornil, J.; Coropceanu, V. Molecular Understanding of Organic Solar Cells: The Challenges. *Acc. Chem. Res.* **2009**, *42*, 1691-1699.
- (22) Clarke, T. M.; Durrant, J. R. Charge Photogeneration in Organic Solar Cells. *Chem. Rev.* **2010**, *110*, 6736-6767.
- (23) Ostroverkhova, O. Organic Optoelectronic Materials: Mechanisms and Applications. *Chem. Rev.* **2016**, *116*, 13279-13412.
- (24) Savoie, B. M.; Jackson, N. E.; Chen, L. X.; Marks, T. J.; Ratner, M. A. Mesoscopic Features of Charge Generation in Organic Semiconductors. *Acc. Chem. Res.* **2014**, *47*, 3385-3394.
- (25) Gelinas, S.; Rao, A.; Kumar, A.; Smith, S. L.; Chin, A. W.; Clark, J.; van der Poll, T. S.; Bazan, G. C.; Friend, R. H. Ultrafast Long-Range Charge Separation in Organic Semiconductor Photovoltaic Diodes. *Science* **2014**, *343*, 512-516.
- (26) Jailaubekov, A. E.; Willard, A. P.; Tritsch, J. R.; Chan, W. L.; Sai, N.; Gearba, R.; Kaake, L. G.; Williams, K. J.; Leung, K.; Rossky, P. J.; Zhu, X. Y. Hot charge-transfer excitons set the time limit for charge separation at donor/acceptor interfaces in organic photovoltaics. *Nat. Mater.* **2013**, *12*, 66-73.
- (27) Zhang, G. C.; Chen, X. K.; Xiao, J. Y.; Chow, P. C. Y.; Ren, M. R.; Kupgan, G.; Jiao, X. C.; Chan, C. C. S.; Du, X. Y.; Xia, R. X.; Chen, Z. M.; Yuan, J.; Zhang, Y. Q.; Zhang, S. F.; Liu, Y. D.; Zou, Y. P.; Yan, H.; Wong, K. S.; Coropceanu, V.; Li, N.; Brabec, C. J.; Bredas, J. L.; Yip, H. L.; Cao, Y. Delocalization of exciton and electron wavefunction in non-fullerene acceptor molecules enables efficient organic solar cells. *Nat. Commun.* **2020**, *11*, 3943.

- (28) McMahon, D. P.; Cheung, D. L.; Troisi, A. Why Holes and Electrons Separate So Well in Polymer/Fullerene Photovoltaic Cells. *J. Phys. Chem. Lett.* **2011**, *2*, 2737-2741.
- (29) Groves, C. Suppression of geminate charge recombination in organic photovoltaic devices with a cascaded energy heterojunction. *Energy Environ. Sci.* **2013**, *6*, 1546-1551.
- (30) Bartelt, J. A.; Beiley, Z. M.; Hoke, E. T.; Mateker, W. R.; Douglas, J. D.; Collins, B. A.; Tumbleston, J. R.; Graham, K. R.; Amassian, A.; Ade, H.; Frechet, J. M. J.; Toney, M. F.; McGehee, M. D. The Importance of Fullerene Percolation in the Mixed Regions of Polymer-Fullerene Bulk Heterojunction Solar Cells. *Adv. Energy Mater.* **2013**, *3*, 364-374.
- (31) Westacott, P.; Tumbleston, J. R.; Shoaee, S.; Fearn, S.; Bannock, J. H.; Gilchrist, J. B.; Heutz, S.; deMello, J.; Heeney, M.; Ade, H.; Durrant, J.; McPhail, D. S.; Stingelin, N. On the role of intermixed phases in organic photovoltaic blends. *Energy Environ. Sci.* **2013**, *6*, 2756-2764.
- (32) Burke, T. M.; McGehee, M. D. How High Local Charge Carrier Mobility and an Energy Cascade in a Three-Phase Bulk Heterojunction Enable > 90% Quantum Efficiency. *Adv. Mater.* **2014**, *26*, 1923-1928.
- (33) Shi, L.; Lee, C. K.; Willard, A. P. The Enhancement of Interfacial Exciton Dissociation by Energetic Disorder Is a Nonequilibrium Effect. *ACS Central Sci.* **2017**, *3*, 1262-1270.
- (34) Govatski, J. A.; da Luz, M. G. E.; Koehler, M. Anomalous maximum and minimum for the dissociation of a geminate pair in energetically disordered media. *Chem. Phys. Lett.* **2015**, *620*, 123-128.
- (35) Zhu, L. Y.; Zhang, J. Q.; Guo, Y.; Yang, C.; Yi, Y. P.; Wei, Z. X. Small Exciton Binding Energies Enabling Direct Charge Photogeneration Towards Low-Driving-Force Organic Solar Cells. *Angew Chem. Int. Ed.* **2021**, *60*, 15348-15353.
- (36) Lee, T. H.; Hillman, S. A. J.; Gonzalez-Carrero, S.; Difilippo, A.; Durrant, J. R. Long-Lived Charges in Y6:PM6 Bulk-Heterojunction Photoanodes with a Polymer Overlayer Improve Photoelectrocatalytic Performance. *Adv. Energy Mater.* **2023**, *13*, 2300400.
- (37) Price, M. B.; Hume, P. A.; Iliina, A.; Wagner, I.; Tamming, R. R.; Thorn, K. E.; Jiao, W. T.; Goldingay, A.; Conaghan, P. J.; Lakhwani, G.; Davis, N. J. L. K.; Wang, Y. F.; Xue, P. Y.; Lu, H.; Chen, K.; Zhan, X. W.; Hodgkiss, J. M. Free charge photogeneration in a single component high photovoltaic efficiency organic semiconductor. *Nat. Commun.* **2022**, *13*, 2827.
- (38) Wang, R.; Zhang, C. F.; Li, Q.; Zhang, Z. G.; Wang, X. Y.; Xiao, M. Charge Separation from an Intra-Moiety Intermediate State in the High-Performance PM6:Y6 Organic Photovoltaic Blend. *J. Am. Chem. Soc.* **2020**, *142*, 12751-12759.
- (39) Jasiunas, R.; Zhang, H. T.; Devizis, A.; Franckevicius, M.; Gao, F.; Gulbinas, V. Thermally Activated Reverse Electron Transfer Limits Carrier Generation Efficiency in PM6:Y6 Non-Fullerene Organic Solar Cells. *Sol. Rrl* **2022**, *6*, 2100963.
- (40) Wang, T.; Kafle, T. R.; Kattel, B.; Chan, W.-L. A Multidimensional View of Charge Transfer Excitons at Organic Donor-Acceptor Interfaces. *J. Am. Chem. Soc.* **2017**, *139*, 4098-4106.
- (41) Perdigon-Toro, L.; Zhang, H. T.; Markina, A. S.; Yuan, J.; Hosseini, S. M.; Wolff, C. M.; Zuo, G. Z.; Stolterfoht, M.; Zou, Y. P.; Gao, F.; Andrienko, D.; Shoaee, S.; Neher, D. Barrierless Free Charge Generation in the High-Performance PM6:Y6 Bulk Heterojunction Non-Fullerene Solar Cell. *Adv. Mater.* **2020**, *32*, 1906763.
- (42) Yao, Y.; Xie, X. Y.; Ma, H. B. Ultrafast Long-Range Charge Separation in Organic Photovoltaics: Promotion by Off-Diagonal Vibronic Couplings and Entropy Increase. *J. Phys. Chem. Lett.* **2016**, *7*, 4830-4835.
- (43) Gregg, B. A. Entropy of Charge Separation in Organic Photovoltaic Cells: The Benefit of Higher Dimensionality. *J. Phys. Chem. Lett.* **2011**, *2*, 3013-3015.

- (44) Hood, S. N.; Kassal, I. Entropy and Disorder Enable Charge Separation in Organic Solar Cells. *J. Phys. Chem. Lett.* **2016**, *7*, 4495-4500.
- (45) Kafle, T. R.; Chan, W. L. Exciton Heating Versus Cooling: Charge Separation Driven by Entropy and Delocalization at Interfaces with Planar Molecules. *Phys. Rev. Appl.* **2021**, *15*, 044054.
- (46) Kafle, T. R.; Kattel, B.; Wanigasekara, S.; Wang, T.; Chan, W. L. Spontaneous Exciton Dissociation at Organic Semiconductor Interfaces Facilitated by the Orientation of the Delocalized Electron-Hole Wavefunction. *Adv. Energy Mater.* **2020**, *10*, 1904013.
- (47) Tu, S. L.; Zhang, L.; Lin, X.; Xiao, L. R.; Wang, W.; Ling, Q. D. Modifying polymer PM6 by incorporating a third component for an enhanced short-circuit current density. *J. Mater. Chem. C* **2022**, *10*, 2026-2033.
- (48) Kafle, T. R.; Kattel, B.; Yao, P.; Zereshki, P.; Zhao, H.; Chan, W. L. Effect of the Interfacial Energy Landscape on Photoinduced Charge Generation at the ZnPc/MoS₂ Interface. *J. Am. Chem. Soc.* **2019**, *141*, 11328-11336.
- (49) Xie, Y. P.; Cai, Y. H.; Zhu, L.; Xia, R. X.; Ye, L. L.; Feng, X.; Yip, H. L.; Liu, F.; Lu, G. H.; Tan, S. T.; Sun, Y. M. Fibril Network Strategy Enables High-Performance Semitransparent Organic Solar Cells. *Adv. Funct. Mater.* **2020**, *30*, 2002181.
- (50) Yao, N. N.; Wang, J. Q.; Chen, Z.; Bian, Q. Z.; Xia, Y. X.; Zhang, R.; Zhang, J. Q.; Qin, L. Q.; Zhu, H. M.; Zhang, Y.; Zhang, F. L. Efficient Charge Transport Enables High Efficiency in Dilute Donor Organic Solar Cells. *J. Phys. Chem. Lett.* **2021**, *12*, 5039-5044.
- (51) Zhang, X. N.; Li, C.; Xu, J. Q.; Wang, R.; Song, J. L.; Zhang, H.; Li, Y. X.; Jing, Y. N.; Li, S. L.; Wu, G. B.; Zhou, J.; Li, X.; Zhang, Y. Y.; Li, X.; Zhang, J. Q.; Zhang, C. F.; Zhou, H. Q.; Sun, Y. M.; Zhang, Y. High fill factor organic solar cells with increased dielectric constant and molecular packing density. *Joule* **2022**, *6*, 444-457.
- (52) Yao, Y. Establishing a microscopic model for nonfullerene organic solar cells: Self-accumulation effect of charges. *J. Chem. Phys.* **2018**, *149*, 194902.
- (53) Rudayni, F.; Rijal K., Fuller N., Chan, W. -L. . Enthalpy-Uphill Exciton Dissociation at Organic/2D Heterostructures Promotes Free Carrier Generation. *Materials Horizons* **2024**, *inpress*, 10.1039/D1033MH01522J.
- (54) Kafle, T. R.; Kattel, B.; Wang, T.; Chan, W.-L. The relationship between the coherent size, binding energy and dissociation dynamics of charge transfer excitons at organic interfaces. *J. Phys.: Condens. Matter* **2018**, *30*, 454001.
- (55) Kerremans, R.; Kaiser, C.; Li, W.; Zarrabi, N.; Meredith, P.; Armin, A. The Optical Constants of Solution-Processed Semiconductors—New Challenges with Perovskites and Non-Fullerene Acceptors. *Adv. Opt. Mater.* **2020**, *8*, 2000319.

Supporting Information

Endothermic Charge Separation Occurs Spontaneously in Non-Fullerene

Acceptor/Polymer Bulk Heterojunction

Kushal Rijal,^{1,*} Neno Fuller,¹ Fatimah Rudayni,^{1,2} Nan Zhang,³ Xiaobing Zuo,⁴ Cindy L. Berrie,⁵ Hin-Lap Yip,^{3,6,7} Wai-Lun Chan^{1,*}

1. Department of Physics and Astronomy, University of Kansas, Lawrence, Kansas 66045, USA
2. Department of Physics, Jazan University, Jazan 45142, Saudi Arabia
3. Department of Materials Science and Engineering, City University of Hong Kong, Tat Chee Avenue, Kowloon, Hong Kong
4. X-ray Science Division, Argonne National Laboratory, Lemont, Illinois 60439, USA
5. Department of Chemistry, University of Kansas, Lawrence, Kansas 66045, USA
6. School of Energy and Environment, City University of Hong Kong, Tat Chee Avenue, Kowloon, Hong Kong
7. Hong Kong Institute for Clean Energy, City University of Hong Kong, Tat Chee Avenue, Kowloon, Hong Kong

*Email: kushalko85@ku.edu, wlchan@ku.edu

I. Additional UPS spectra

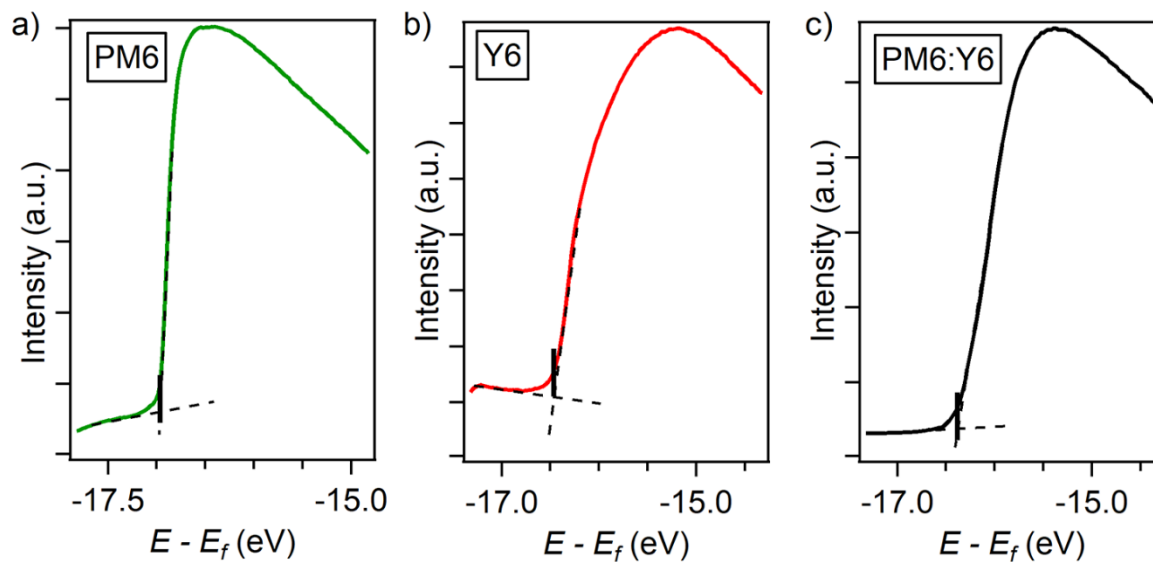


Fig. S1: The UPS spectra for (a) PM6, (b) Y6, and (c) PM6:Y6 blend films near the SECO region. The SECO position for each spectrum is indicated by the solid black line.

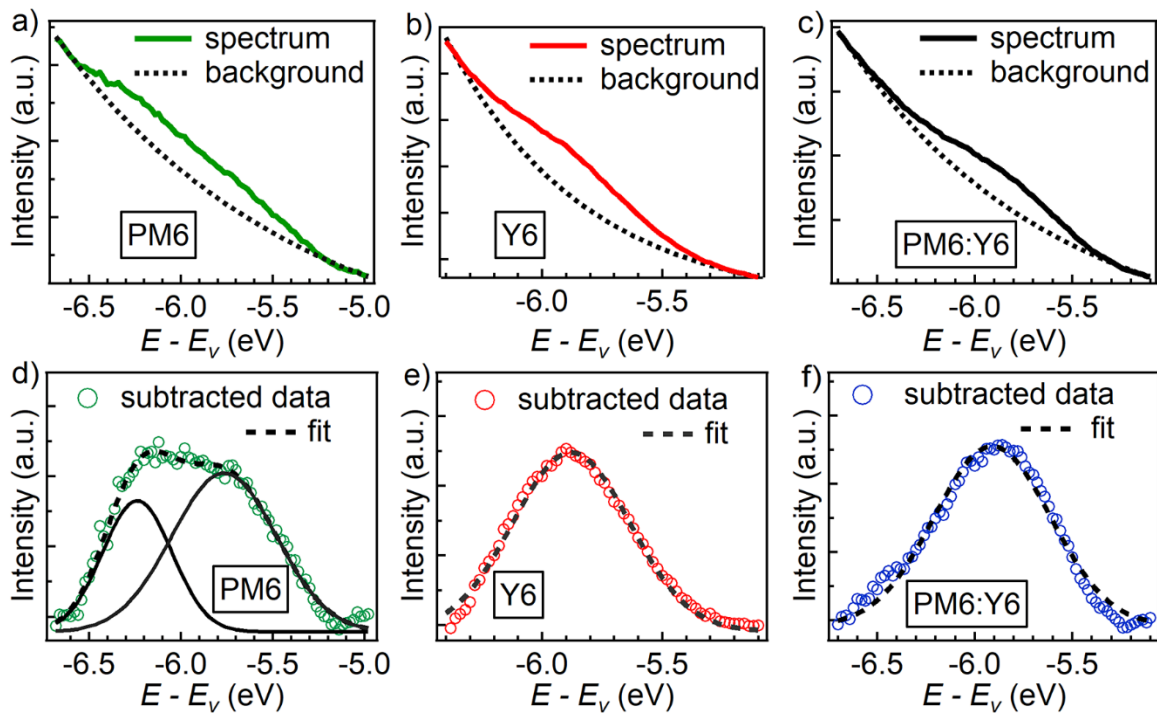


Fig. S2: The HOMO peak of (a & d) PM6, (b & e) Y6 and (c & f) PM6:Y6 blend. The energy is referenced with respect to the vacuum level (E_v). The dotted curves in a, b & c represent the background originated from inelastic photoelectrons. To determine the HOMO peak position, we subtract the background from the raw spectrum. The subtracted data and the gaussian fits are shown in d, e & f. The gaussian peak obtained from the fits corresponds to the HOMO level for each film. For PM6, two peaks are found. The higher energy peak is taken as the HOMO.

Sample	Work function	HOMO energy with respect to the E_v	Lowest Optical Absorption peak
PM6	4.26 eV	-5.76 eV	615 nm (2.02 eV)
Y6	4.76 eV	-5.88 eV	836 nm (1.48 eV)
PM6:Y6 blend	4.86 eV	-5.91 eV	822 nm (1.51 eV)

Table S1: A summary for work function, HOMO position and optical bandgap for all samples.

II. Additional TR-TPPE data

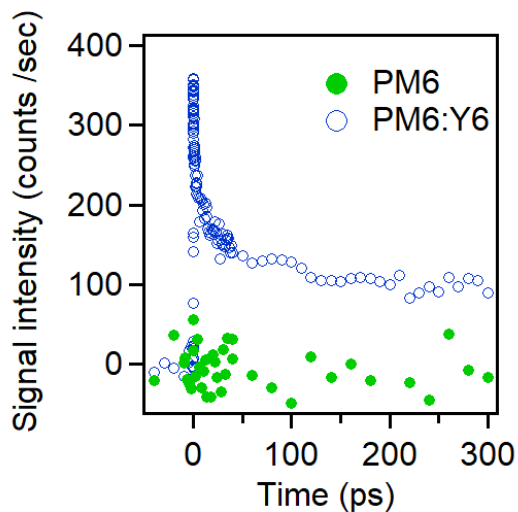


Fig. S3: TR-TPPE signal from PM6 and PM6:Y6 blend films with 780nm excitation. PM6 films do not show signal.

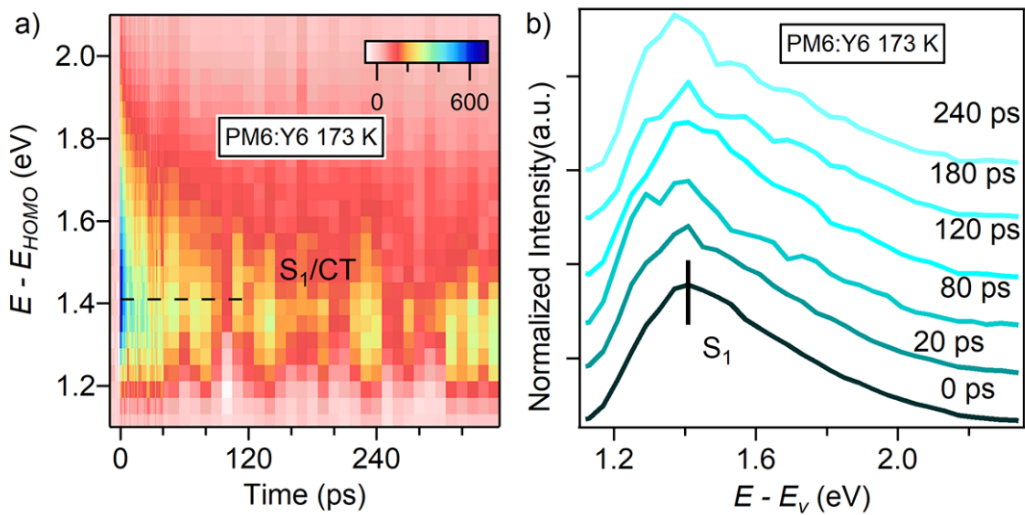


Fig. S4: (a) The TR-TPPE spectrum of PM6:Y6 blend collected at 173 K. No energy uphill CS is observed. (b) Vertical cut of the TR-TPPE spectra at different delay times.

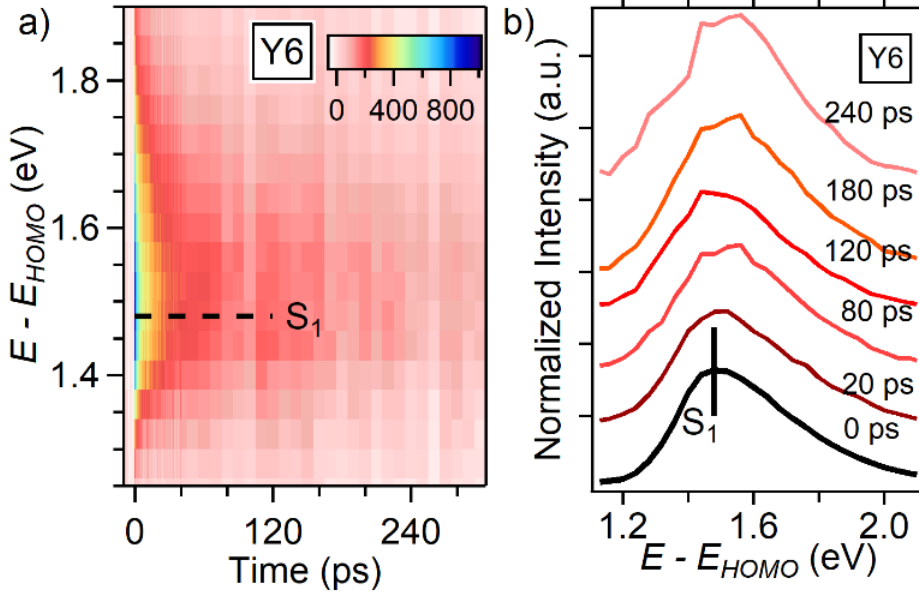


Fig. S5: (a) TR-TPPE spectrum of Y6 film collected at room temperature with a pump wavelength of 780nm. Population in S_1 states continuously decays throughout the time. No energy uphill CS is observed. (b) Vertical cuts of the spectra from (a) at different time delays.

III. Derivation of Eq. (2) in the main text

The binding energy of Y6's S_1 exciton ($Ex_b^{S_1}$) and the CT exciton (Ex_b^{CT}) can be written as:

$$Ex_b^{S_1} = (E_{LUMO}^{Y6} - E_{HOMO}^{Y6}) - E_{S_1}^{Y6}, \text{ and} \quad (S1)$$

$$Ex_b^{CT} = (E_{LUMO}^{Y6} - E_{HOMO}^{PM6}) - E_{CT}. \quad (S2)$$

In these two equations, E_{LUMO}^{Y6} , E_{HOMO}^{Y6} , and E_{HOMO}^{PM6} are the Y6's LUMO, Y6's HOMO and PM6's HOMO energies, respectively. $E_{S_1}^{Y6}$ and E_{CT} are the energy of the Y6's S_1 exciton and the energy of the CT exciton, respectively.

Subtracting Eq. (S2) and (S1), we can get the difference between the two binding energies:

$$Ex_b^{S_1-CT} = Ex_b^{S_1} - Ex_b^{CT} = (E_{HOMO}^{PM6} - E_{HOMO}^{Y6}) - (E_{S_1}^{Y6} - E_{CT}), \quad (S3)$$

which is same as the Eq. (2) in the main text.

IV. Additional X-ray scattering data and fitting

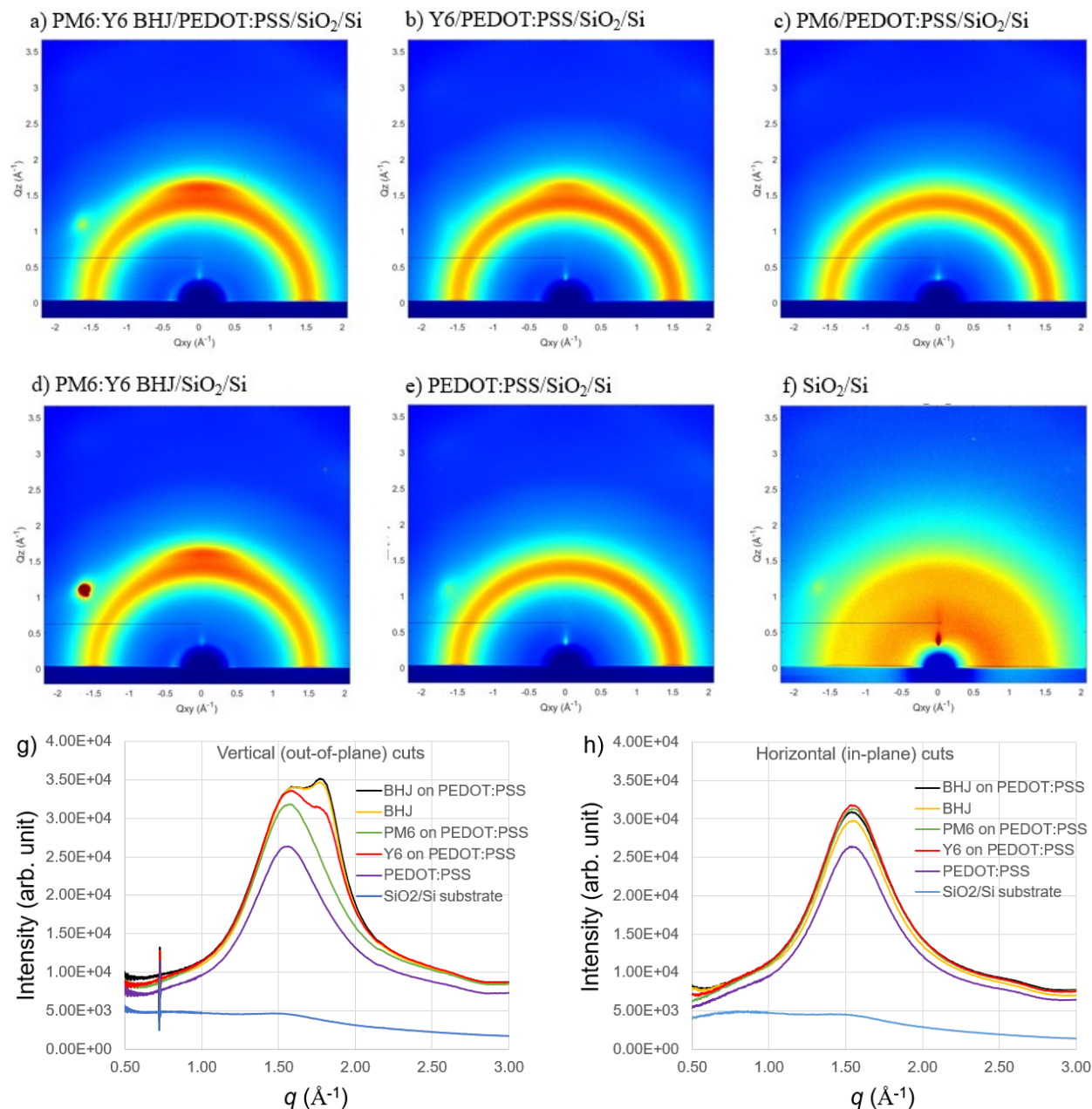


Fig. S6: The GIWAXS patterns of (a) PM6:Y6 BHJ/PEDOT:PSS/SiO₂/Si, (b) Y6/PEDOT:PSS/SiO₂/Si, (c) PM6/PEDOT:PSS/SiO₂/Si, (d) PM6:Y6 BHJ/SiO₂/Si, (e) PEDOT:PSS/SiO₂/Si, and (f) SiO₂/Si samples. The vertical (out-of-plane) and horizontal (in-plane) cuts of these GIWAXS patterns ((a) to (f)) are shown in (g) and (h), respectively.

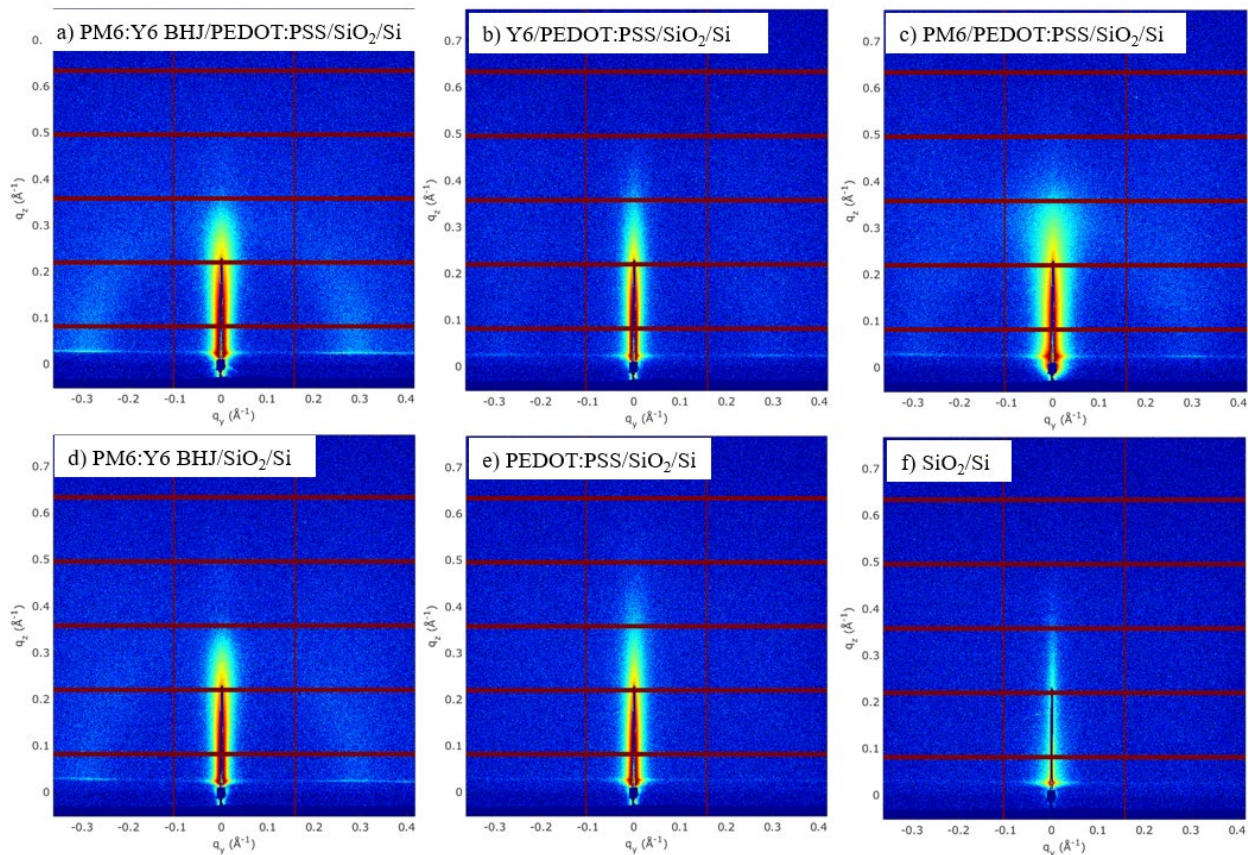


Fig. S7: The GISAXS patterns of (a) PM6:Y6 BHJ/PEDOT:PSS/SiO₂/Si, (b) Y6/PEDOT:PSS/SiO₂/Si, (c) PM6/PEDOT:PSS/SiO₂/Si, (d) PM6:Y6 BHJ/SiO₂/Si, (e) PEDOT:PSS/SiO₂/Si, and (f) SiO₂/Si samples.

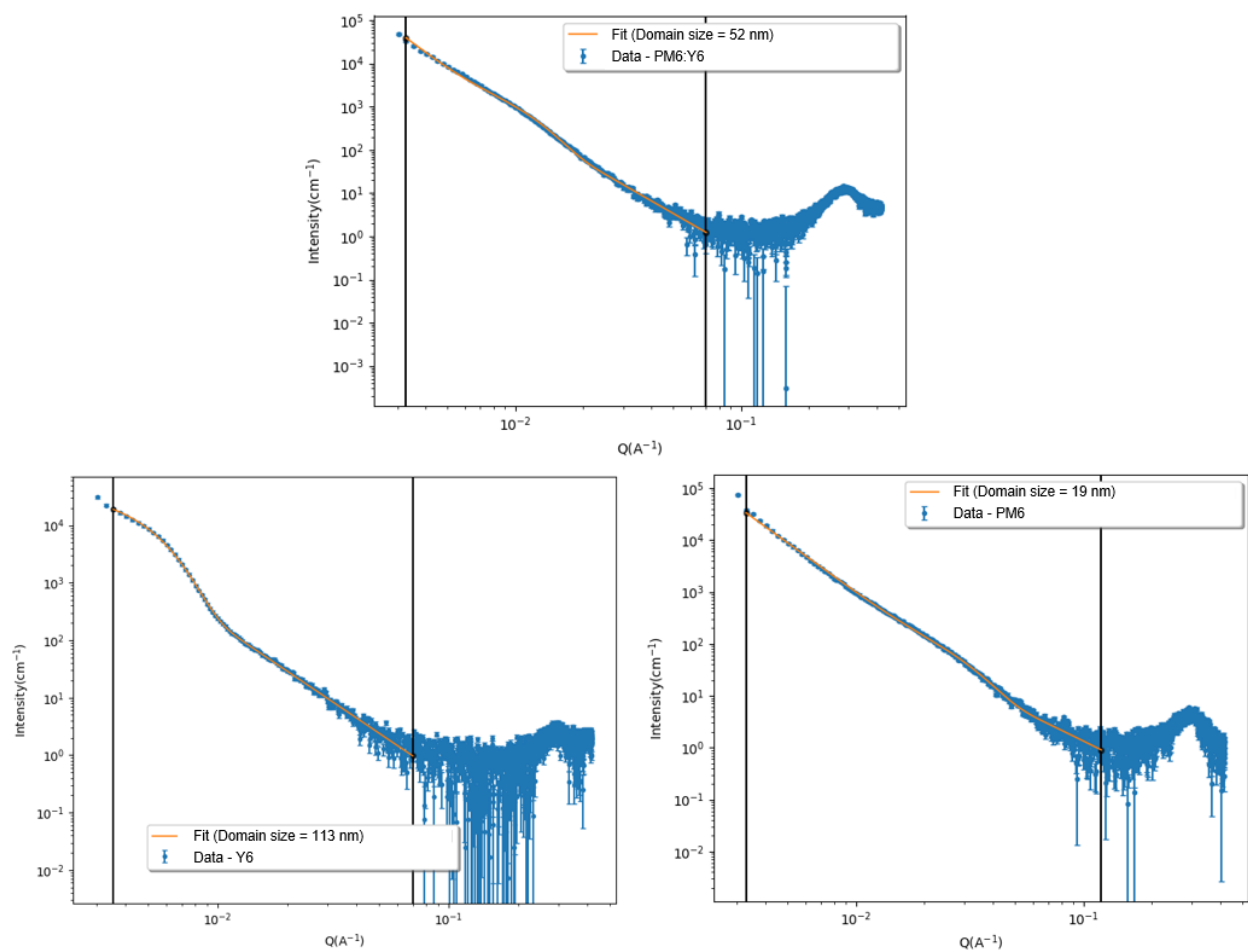


Fig. S8: Fits for the GISAXS horizontal linecut for the PM6:Y6, Y6, and PM6 samples. The background of the substrate was first subtracted from sample GISAXS linecuts. Then, they are fitted with SAXS unified model^{S1} using program SasView [<https://www.sasview.org/>]. The domain size was estimated using the R_g value obtained from unified model fitting and the sphere shape approximation.

V. Additional AFM data

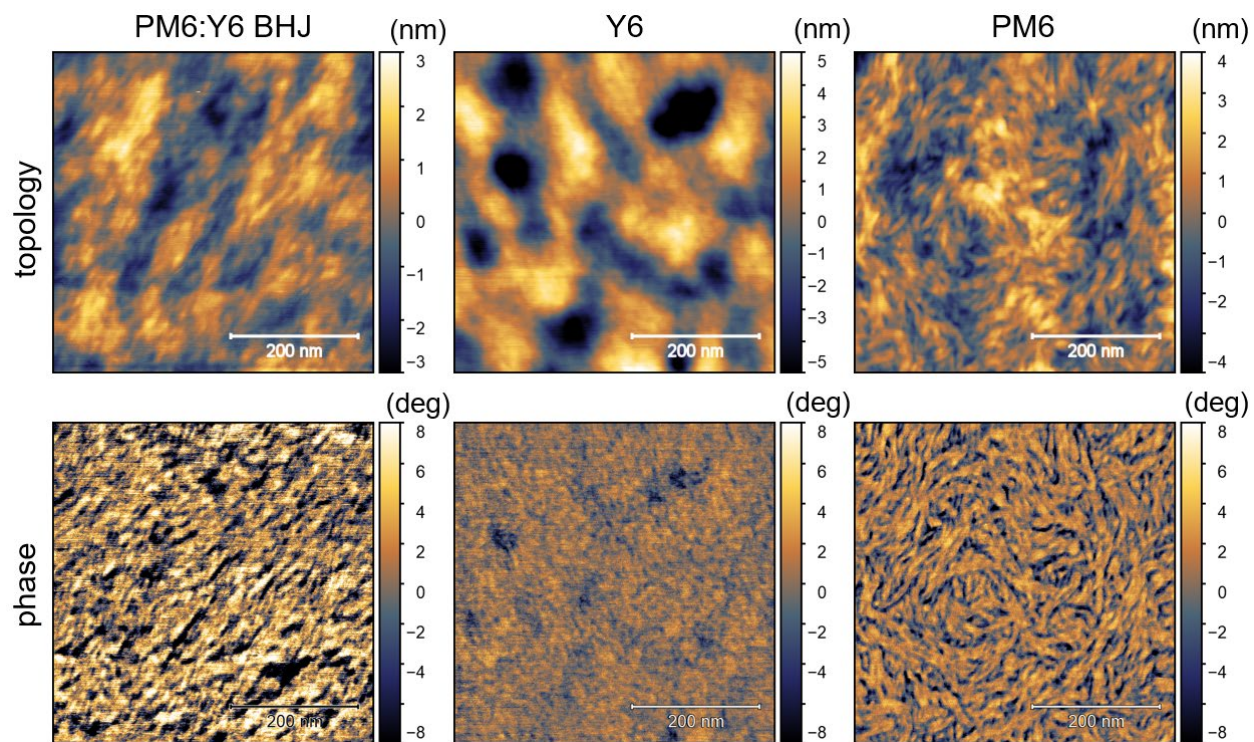


Fig. S9: The topology and phase images of PM6:Y6 BHJ, Y6 and PM6 samples.

VI. Estimation of the excitation density

The excitation density (ρ) was estimated using the following formula:

$$\rho = \frac{J \times \alpha \times (1 - R)}{h\nu}$$

, where J , α , R , and $h\nu$ are the incident fluence of the pump pulse, optical absorption constant, reflectivity, and the pump photon energy, respectively. In our experiment, for an incidence angle of 30° , J was $10.15 \mu\text{J cm}^{-2}$. The central wavelength of the pump pulse λ was 780 nm. At this wavelength, the attenuation coefficient, and the refractive index of the PM6:Y6 film were taken to be $k \approx 1.2$, and $n \approx 2.2$ respectively. Note that the mixing ratio of our PM6:Y6 BHJ sample is (1:3). To arrive at the above n and k , we took the averaged values of n and k for the neat-Y6 and PM6:Y6 (1:1.2) reported in Ref. 55 cited in the main text.

The absorption constant α was calculated using the formula:

$$\alpha = \frac{4\pi \times k}{\lambda}$$

The α at 780 nm is calculated to be $1.93 \times 10^5 \text{ cm}^{-1}$.

R was calculated using the Fresnel equation (for p-polarized light) [Ref. S2]:

$$R = \frac{\left| n_2^2 \cos \theta - n_1 \sqrt{n_2^2 - (n_1 \sin \theta)^2} \right|^2}{\left| n_2^2 \cos \theta + n_1 \sqrt{n_2^2 - (n_1 \sin \theta)^2} \right|^2}$$

, where $\theta = 30^\circ$ is the angle of incidence, $n_1 = 1$ is the refractive index of the incident medium (vacuum), and $n_2 = n + ik$ is the complex refractive index of the organic film.

The calculated R is 0.2.

Using the above equations, we estimate that $\rho \sim 6.2 \times 10^{18} \text{ cm}^{-3}$.

References

S1: Beaucage, G. (2012). Combined Small-Angle Scattering for Characterization of Hierarchically Structured Polymer Systems over Nano-to-Micron Meter: Part II Theory. In Polymer Science: A Comprehensive Reference (M, MKaM, ed.), Vol. 2, pp. 399. Elsevier, Amsterdam.

S2: Jackson, J. D. (1998). Classical Electrodynamics, Third Edition, pp. 306. John Wiley & Sons, Inc., New York.